Journal of Colloid and Interface Science 650 (2023) 2056–2064

Contents lists available at ScienceDirect

Journal of Colloid And Interface Science

journal homepage: www.elsevier.com/locate/jcis

# Immobilization of iron phthalocyanine on MOF-derived *N*-doped carbon for promoting oxygen reduction in zinc-air battery

Anrui Dong [a,1], Yu Lin [c,1], Yuanyuan Guo [a], Dandan Chen [a], Xian Wang [a], Yongjie Ge [a], Qipeng Li [b,*], Jinjie Qian [a,*]

[a] Key Laboratory of Carbon Materials of Zhejiang Province, College of Chemistry and Materials Engineering, Wenzhou University, Wenzhou, Zhejiang 325035, PR China
[b] College of Chemistry and Chemical Engineering, Zhaotong University, Zhaotong, Yunnan 657000, PR China
[c] Comprehensive Technical Service Center of Wenzhou Customs, Wenzhou, 325000, PR China

## HIGHLIGHTS

- One Zn-based pillar-layer MOF nanosheet is easily achieved by its restricted axial growth.
- Iron phthalocyanines could be firmly immobilized into MOF-derived porous Ndoped carbons.
- The optimal catalyst of FePc@NC-1000 shows high oxygen reduction activity and durability.

## GRAPHICAL ABSTRACT

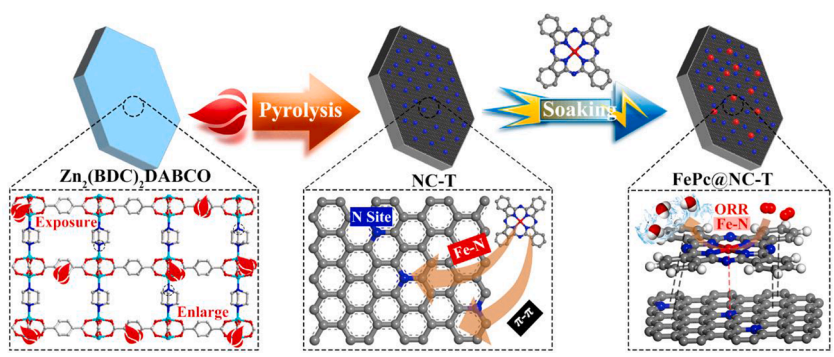


## ARTICLE INFO

*Keywords:*
Metal-organic framework
Carbon nanosheet
Fe phthalocyanine
Oxygen reduction
Zinc-air battery

## ABSTRACT

Functional carbon nanomaterials play a crucial role in the cathodic oxygen reduction reaction (ORR) for sustainable fuel cells and metal-air batteries. In this study, we propose an effective approach to immobilize iron phthalocyanines (FePc) by employing a porous *N*-doped carbon material, denoted as **NC-1000**, derived from a sheet-shaped coordination polymer. The resulting **NC-1000** possesses substantial porosity and abundant pore defects. The nitrogen sites within **NC-1000** not only facilitate FePc adsorption but also optimize the electron distribution at the Fe-N site.

The **FePc@NC-1000** composite material exhibits a significant number of active centers in the form of Fe-$N_4$ moieties, showcasing satisfactory ORR activity. Specifically, it demonstrates an onset potential of 0.99 V, a positive half-wave potential of 0.86 V, a large limiting current of 5.96 mA $cm^{-2}$, and a small Tafel slope of 44.41 mV $dec^{-1}$. Additionally, theoretical calculations and experimental results confirm the favorable performance and durability of zinc-air batteries assembled using **FePc@NC-1000**, thereby highlighting their considerable potential for practical applications. Overall, this study provides a comprehensive exploration of the enhanced catalytic performance and increased stability of metal–organic framework-derived functional carbon nanomaterials as cost-effective, efficient, and stable catalysts for the ORR.

* Corresponding authors.
*E-mail addresses:* qpli@ztu.edu.cn (Q. Li), jinjieqian@wzu.edu.cn (J. Qian).
[1] These authors contributed equally to this work.

https://doi.org/10.1016/j.jcis.2023.06.043
Received 23 March 2023; Received in revised form 17 May 2023; Accepted 8 June 2023
Available online 13 June 2023

## 1. Introduction

With the rapid development of modern human society, addressing the growing energy demand has become imperative [1,2]. However, the excessive use of fossil fuels has resulted in the generation of substantial greenhouse gases, posing significant threats to the environment and human health [3]. In the context of China's high-quality development direction and "dual carbon" goals, there is vast potential for clean energy conversion and storage technologies. The urgent need to harness green renewable energy to alleviate energy shortages and environmental pollution has become increasingly apparent. In recent years, hydrogen–oxygen fuel cells and secondary batteries have emerged as viable solutions [4–6]. However, the oxygen reduction reaction (ORR), which is inherent to these energy conversion systems, exhibits sluggish 4-electron transport on the cathode. Platinum (Pt)-based nanomaterials have been considered the best catalysts for the ORR nonetheless, their scarcity and poor stability hinder widespread applications [7,8]. Therefore, there is a growing interest in the development of low-cost, high-performance, and durable non-Pt catalysts.

Microporous metal–organic frameworks (MOFs), comprising inorganic metals and organic ligands, have been extensively explored for the fabrication of various ORR catalysts [9–11]. Due to their high carbon content, MOF materials have emerged as promising precursors for cost-effective carbon-based catalysts [12,13]. These MOF derivatives exhibit excellent physicochemical properties, owing to their high porosity, unique nanostructures, tunable morphologies, and abundant active species. Although researchers have achieved effective control over the formation of hierarchical pores in MOF-derived carbon nanomaterials, the synthesis process remains challenging. The pyrolysis of Zn-based MOFs offers a facile approach to obtain porous carbons, as Zn species have a low boiling point [14]. Therefore, the exploration of simplified surface modifications to achieve the desired structure and morphology of MOF derivatives, resulting in pores with increased active sites for the ORR, holds significant value.

Atomically dispersed Fe-$N_x$ sites have been identified as efficient catalysts for the ORR [15,16]. In particular, molecular metal phthalocyanine (MPc) exhibits attractive properties due to its tunable electronic structure and compatibility with various substrates [17,18]. However, the plane-symmetric structure of MPc hinders the favorable distribution of electrons around the metal center, thus affecting reactant adsorption [19]. Moreover, the active site's central metal atom tends to separate from the MPc during catalytic operations, leading to poor electrochemical stability [20]. Hence, the introduction of MPc species into porous *N*-doped carbon substrates represents an effective strategy to overcome these limitations, as it disrupts the electron symmetry distribution at the metal sites and facilitates reactant binding, thereby enhancing MPc stability [21]. Consequently, the rational design and facile preparation of MOF-derived carbon nanomaterials capable of effectively encapsulating MPc molecules for efficient ORR catalysis present a significant challenge.

Herein, a zinc-based pillar-layer coordination polymer with *N*-containing linkers and a hexagonal morphology was thermally transformed into *N*-doped carbon, serving as a host matrix for anchoring iron phthalocyanines (FePc) (Scheme 1). Firstly, sheet-shaped **$Zn_2$(BDC)$_2$DABCO** was obtained, with its axial growth being restricted. Subsequently, the resulting MOF nanosheets were subjected to pyrolysis at 1000 °C, resulting in the formation of porous *N*-doped carbon (**NC-1000**) with large pores, abundant defects, and appropriate graphitization. Finally, FePc was effectively confined within the MOF-derived porous *N*-doped carbon through Fe-N interactions and π-π stacking, leading to the formation of the final product of **FePc@NC-1000**. The obtained **FePc@NC-1000** exhibited favorable chemical stability, high conductivity, and efficient catalytic activity for the ORR in zinc-air batteries (ZABs), demonstrating performance comparable to that of commercial 20% Pt/C.

## 2. Experimental section

### 2.1. Materials

All chemicals and reagents are of analytical grade and obtained commercially without further purification. Zinc acetate ($Zn(CH_3COO)_2{\cdot}2H_2O$), triethylenediamine (DABCO), 1,4-dicarboxybenzene ($H_2BDC$) N,*N*-Dimethylformamide (DMF), FePc, distilled water, 20 wt% Pt/C, and 5 wt% Nafion ionomer solution were obtained from Johnson Matthey Fuel Cells NA and DuPont, USA, respectively. Pure argon was used in the experiments.

### 2.2. Synthesis of $Zn_2$(BDC)$_2$DABCO

Firstly, 29.4 mg (0.16 mM) $Zn(CH_3COO)_2{\cdot}2H_2O$, 31.1 mg (0.16 mM) $H_2BDC$, and 9.5 mg (0.08 mM) DABCO were dispersed in 5 ml DMF and transferred to a 25 ml vial. The vial was placed in an oven at 85 °C for three hours at 800 rpm. Finally, it was centrifuged, washed with DMF, and dried at 80 °C overnight. **$Zn_2$(BDC)$_2$DABCO** was obtained as a white powder.

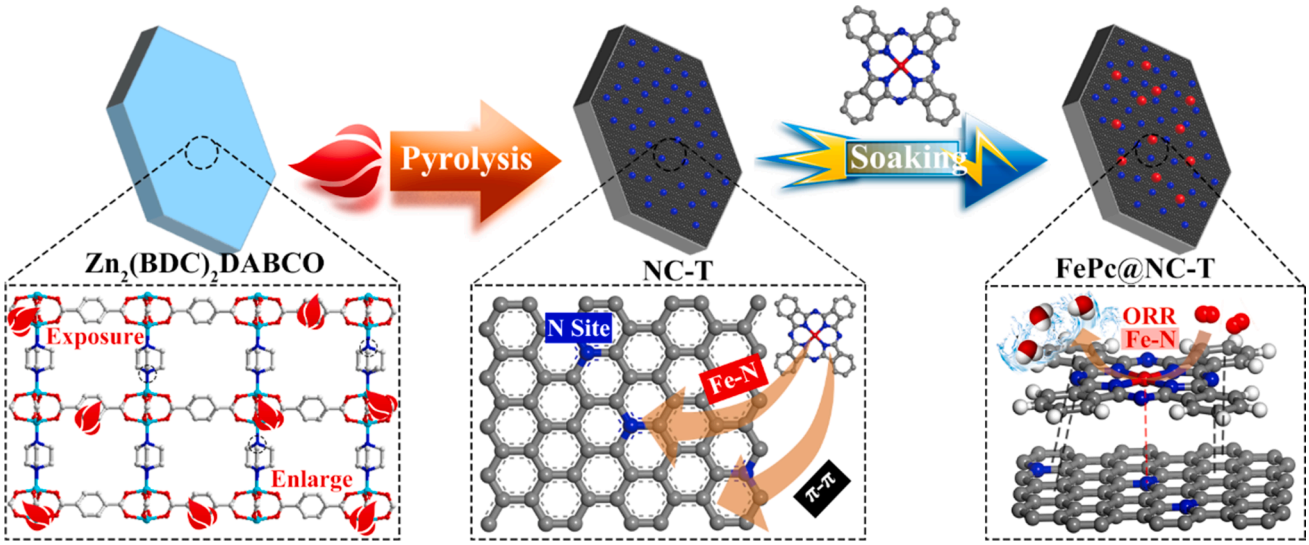


**Scheme 1.** The synthesis route to produce efficient ORR electrocatalyst of the **FePc@NC-T** series.

### 2.3. Synthesis of NC-600/800/1000

The synthesized **$Zn_2(BDC)_2DABCO$** was placed in an open quartz protective tube. The open tube was then inserted into a CVD tube furnace. Finally, the samples were calcined at 600/800/1000 °C for 2 h with a heating rate of 10 °C $min^{-1}$ under an Ar atmosphere to obtain **NC-600/800/1000**.

### 2.4. Synthesis of FePc@NC-600/800/1000

FePc (5 mg) and **NC-600/800/1000** (10 mg) were combined in 5 ml DMF and stirred overnight. Finally, the mixture was centrifuged, washed with DMF, and dried overnight at 80 °C. **FePc@NC-600/800/1000** was obtained as a black powder.

## 3. Results and discussion

As shown in Fig. 1a, **$Zn_2(BDC)_2DABCO$** nanosheets were synthesized using $H_2BDC$, DABCO as organic ligands, and Zn(II) ions as metal nodes (Fig. S1a, Table S1) [22]. Initially, the 2D square-grid of $\{Zn_2(BDC)_2\}_n$ was formed by Zn paddle-wheel secondary building units and deprotonated $BDC^{2-}$ linkers (Fig. S1b). Subsequently, the terminal sites of the Zn paddle wheels were further extended into a 3D network by bridging DABCO pillars (Fig. S1c and S1d). The powder X-ray diffraction (PXRD) pattern of the pristine MOFs exhibited consistency with the simulated pattern [22], indicating their high crystallinity and purity (Fig. 1b). The four discernible diffraction peaks at 8.30°, 9.18°, 11.74°, and 12.38° were indexed to the (100), (001), (110), and (101) crystal planes, respectively. The resulting MOF samples contained ultrathin nanosheets (Fig. 1b inset, S2 and S3). Atomic force microscopy (AFM) is generally used to measure the thicknesses of 2D materials. The AFM results demonstrated that the obtained **$Zn_2(BDC)_2DABCO$** possessed an ultrathin morphology (Fig. S3) with an average thickness of 100–150 nm. The SEM images of **$Zn_2(BDC)_2DABCO$** from various angles (Fig. S2, side view) confirmed the ultrathin morphology consistent with the AFM profiles. Fig. 1c exhibited type-IV $N_2$ isotherms, indicating the presence of micro/mesopores, in line with the pore size distribution curve (Fig. S4). However, the $N_2$ adsorption capacity was relatively low due to the lack of coordination between the inorganic metal nodes in the MOFs and the organic ligands, resulting in an unsaturated coordination number. Nevertheless, some solvent molecules (e.g., $H_2O$, DMF, DMA, ethanol, and methanol) coordinated with the inorganic nodes, achieving a saturated coordination number. Solvent molecules with high boiling points, such as DMF and DMA, pose challenges during the desolvation process as they could not be easily removed from the MOF samples [23]. MOFs exhibit high porosity and are capable of encapsulating solvent molecules (e.g., $H_2O$). However, when solvents with high boiling points are present, their removal during the drying process becomes difficult [24], leading to a decrease in MOF porosity and subsequently lower adsorption. The thermogravimetric analysis (TGA) in Fig. 1d revealed that the initial weight loss rate reached 21% at 400 °C, while the main framework gradually decomposed, resulting in a mass retention of 37% at 500 °C.

The MOF nanosheets obtained were subjected to pyrolysis under an Ar atmosphere to facilitate the anchoring of FePc molecules (Fig. 2a). The *N*-doped carbon nanomaterial of **NC-T** was prepared by pyrolyzing **$Zn_2(BDC)_2DABCO$** at different temperatures. The SEM images (Fig. 2b and S5) revealed a gradual deterioration in the morphology of the MOF precursor with increasing temperature.The size of **NC-T** decreases progressively, and its morphology becomes more irregular. Simultaneously, the zinc species gradually evaporate as the temperature rises. Subsequently, the pyrolyzed **NC-T** series was immersed in a FePc solution and firmly fixed on a carbon skeleton through Fe-N interaction and $\pi$-$\pi$ stacking to prepare **FePc@NC-T**. High-resolution transmission electron microscopy (HR-TEM) images in Fig. 2c and S6 showed an amorphous material with short-range ordered carbons, whereas the derived **FePc@NC-1000** retained its initial morphology and nanostructure (Fig. 2f and S7). Moreover, single-atom Fe species were observed in the aberration-corrected high-angle annular dark-field scanning TEM (AC-HAADF-STEM) images of **FePc@NC-1000** in Fig. 2g and S8. This suggests that the FePc molecules were well-dispersed throughout the hierarchical pores of the MOF-derived carbon materials. Furthermore,

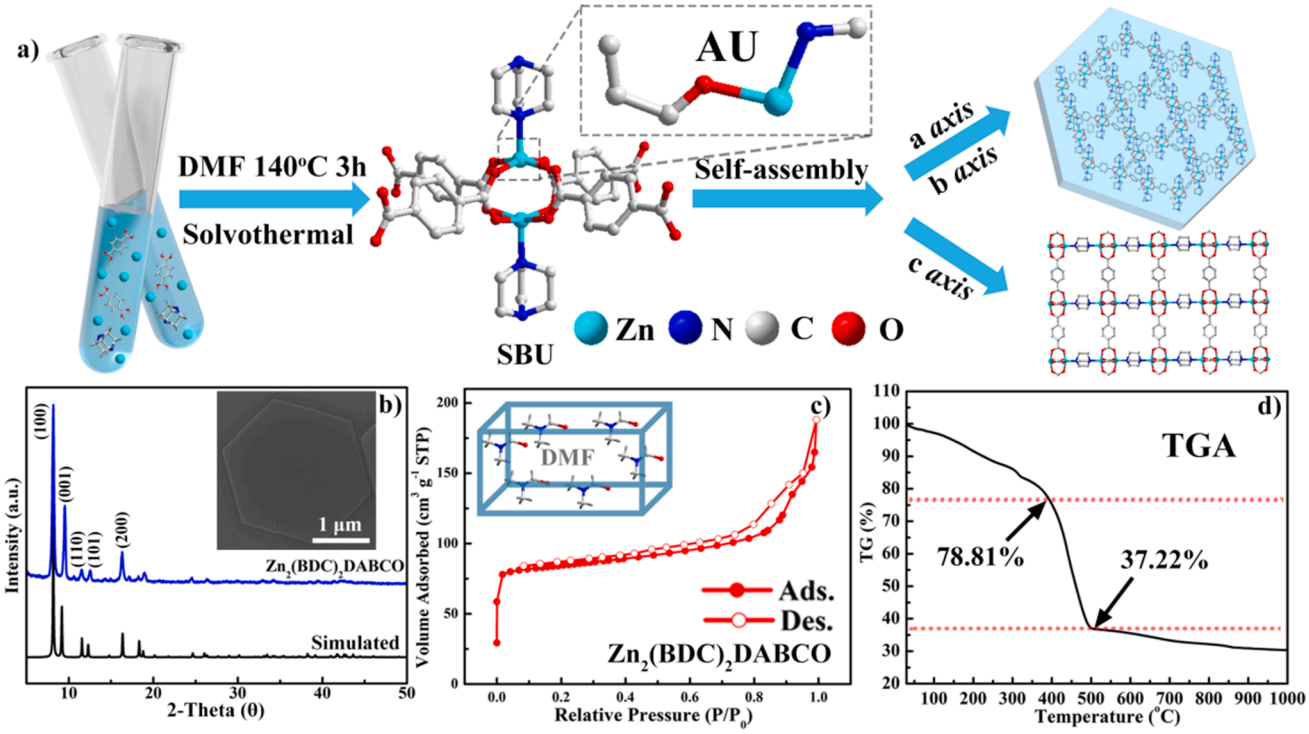


**Fig. 1.** (a) The schematic route to obtain ultrathin MOFs. (b) PXRD patterns, (c) $N_2$ isotherm curves (the inset is the topological structure containing DMF), (d) TGA profile of **$Zn_2(BDC)_2DABCO$**.

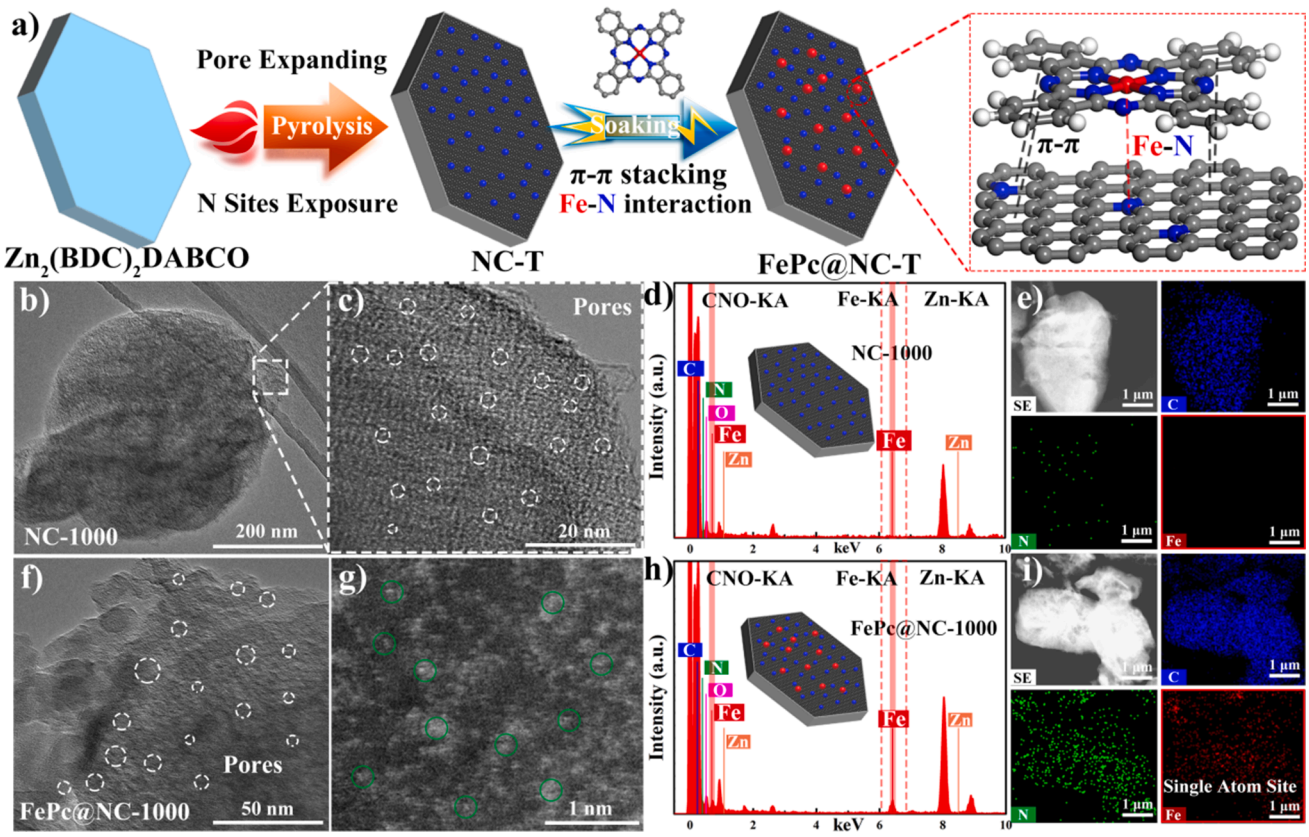


**Fig. 2.** (a) Stepwise synthesis of **FePc@NC-T.** (b) TEM image, (c) HR-TEM image, (d) EDS curve, (e) elemental mapping images of **NC-1000.** (f) TEM image, (g) AC-HAADF-STEM image, (h) EDS curve, (i) elemental mapping images of **FePc@NC-1000**.

comparative analysis of energy-dispersive X-ray spectroscopy (EDS), HAADF-STEM, and the corresponding elemental mapping images demonstrated the uniform doping of Fe and N across the entire **FePc@NC-1000**, without any apparent aggregation of Fe nanoparticles (Fig. 2d-e, h-i)). The atomic percentages of **NC-T** and **FePc@NC-1000** indicate a slight increase in the iron and nitrogen components in **FePc@NC-1000** after soaking, confirming the successful introduction of FePc molecules into **NC-1000** (Table S2).

The phases and pore structures of the obtained MOF-derived nanocomposites were investigated. The PXRD patterns of **NC-600/-800** and their FePc-loaded derivatives revealed three peaks at 31.77°, 34.42°, and 36.26° for the (1 0 0), (0 0 2), and (1 0 1) planes of ZnO, respectively (Fig. 3a, S9) [25]. However, ZnO was not detected in both**NC-1000** and **FePc@NC-1000**, indicating the formation of large pores and abundant N sites for effective FePc anchoring. **FePc@NC-1000** exhibited a broad peak at approximately 28°, suggesting partial graphitization of the carbon matrix. This increased the binding force between **NC-1000** and FePc and facilitated electron mass transfer [26]. Secondly, as shown in Fig. 3b, all **FePc@NC-T** samples exhibited characteristic infrared signals associated with FePc, including Fe-N, C═N, C═C, and C—H bonds. Furthermore, the $I_D/I_G$ values of all the samples were close to 1.00, indicating a similar degree of graphitization and the presence of abundant defect sites (Fig. 3c and S10). The structural defects increased with increasing pyrolysis temperature due to the effective volatilization of zinc species. Similarly, the specific surface areas of **NC-T** and **FePc@NC-T** increased with the formation of pores (Fig. 3d, S11, S12; Table S3). **FePc@NC-1000** exhibited a larger hysteresis loop and a higher abundance of mesopores, which are beneficial for efficient mass transport during the catalytic process.

The surface chemical state and coordination environment of the elements were further investigated using X-ray photoelectron spectroscopy (XPS). The full survey spectra in Fig. 4a confirmed the presence of C, N, and O in both nanocomposites. The deconvoluted C 1s spectra exhibited three peaks at 284.6, 288.8, and 286.1 eV, corresponding to C—C/C═C, C—O, and C—N, respectively. The intensity of the C—N peak in **FePc@NC-1000** was slightly stronger than that in **NC-1000**, indicating successful loading of FePc (Fig. 4b) [27]. The broad peak in the high-resolution N 1s spectra in Fig. 4c predominantly originated from oxidized-N (404.0 eV), graphitic/pyrrolic-N (400.9 eV), and pyridinic-N (398.4 eV) [28,29]. A small fraction of Fe-N bonds was effectively detected in **FePc@NC-1000**, which is considered as optimal catalytic sites for the ORR. Spin-orbit splitting of the Fe $2p_{1/2}$ (722.5 eV) and $2p_{3/2}$ (709.8 eV) peaks was observed in the deconvoluted Fe 2p spectrum of FePc@NC-1000 (Fig. 4d) [30,31]. Weak Zn $2p_{1/2}$ (1045.1 eV) and $2p_{3/2}$ (1022.1 eV) peaks were present in both **NC-1000** and **FePc@NC-1000**, indicating the low amount of non-volatilized Zn species (Fig. 4e). Lastly, the high-resolution O 1s spectra displayed two subpeaks corresponding to C—O and C═O in both carbon nanomaterials, suggesting a similar oxygen coordination environment, as shown in Fig. 4f [32].

Because of its unique porous carbon nanostructure with abundant Fe-N4 species, the electrochemical ORR performance of the **FePc@NC-T** series was investigated. The ORR selectivity was first assessed, and the reduction peak potential of FePc@NC-1000 was found to be 0.92 V, close to Pt/C (0.93 V), and significantly higher than **FePc@NC-600/800** (0.76/0.90 V), **NC-1000** (0.85 V), and FePc (0.80 V) (Fig. 5a). **FePc@NC-1000** also exhibited a higher diffusion-limited current density (JL) of 5.96 mA $cm^{-2}$ compared to FePc, **FePc@NC-600/800**, **NC-1000**, and Pt/C (0.67, 4.14/4.58, 4.26, 5.11 mA $cm^{-2}$) respectively (Fig. 5b). Moreover, it displayed a higher half-wave potential ($E_{1/2}$) and onset potential ($E_{onset}$) of 0.86/0.99 V, surpassing those of **FePc@NC-600** (0.76/0.91 V), **FePc@NC-800** (0.85/0.97 V), and recently reported Fe-based catalysts (Table S4). Additionally, the Koutecky-Levich curves of the **FePc@NC-T** samples demonstrated nearly linear relationships

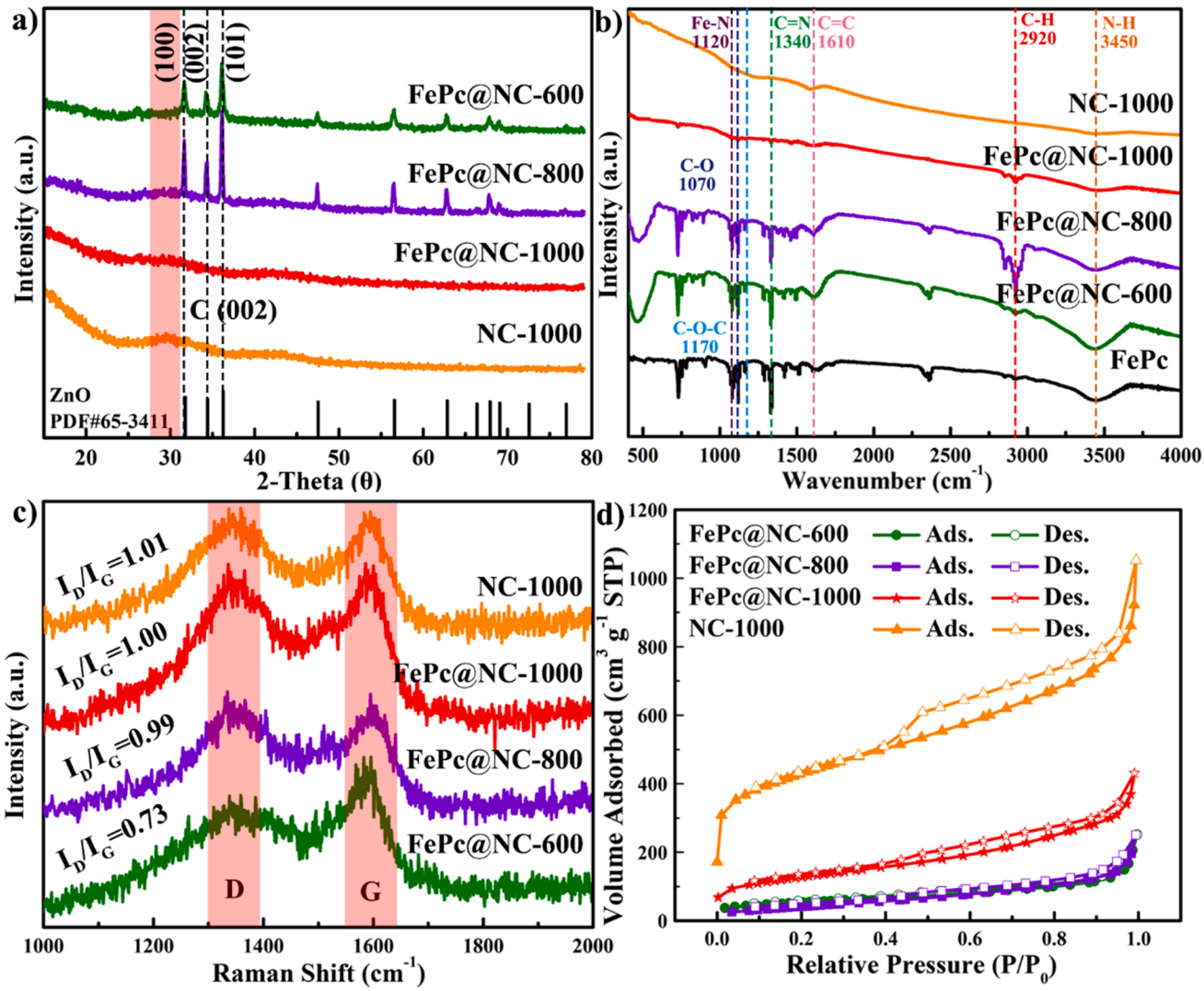


**Fig. 3.** (a) PXRD patterns, (b) FT-IR spectra, (c) Raman spectra, (d) $N_2$ isotherms of the **NC-1000** and **FePc@NC-T** series.

within the range of 0.3–0.7 V (Figs. S13 and S14). Fig. 5c illustrated that **FePc@NC-1000** (44.41 mV $dec^{-1}$) had the smallest Tafel slope, indicating faster reaction kinetics compared to Pt/C (67.09 mV $dec^{-1}$) and FePc (79.65 mV $dec^{-1}$). Moreover, the calculated number of transferred electrons (n: 3.67–3.99) and lower $HO_2^-$ yields (<20%) indicated that all samples exhibited high selectivity through an ideal 4e pathway (Fig. 5d) [33]. The EIS analysis in Fig. 5e revealed that the optimal **FePc@NC-1000** exhibited lower charge transfer resistance with 12.77 Ω, consistent with the aforementioned Tafel results. The double-layer capacitance ($C_{dl}$) of **FePc@NC-1000** (28.66 mF $cm^{-2}$) was also larger than that of **FePc@NC-600/800**, **NC-1000**, Pt/C, and FePc (4.86/11.02, 11.89, 21.24, 0.14 mF $cm^{-2}$), indicating it had the most active sites (Fig. 5f, S15, S16). Fig. 5f demonstrated that compared to Pt/C (89.30%), **FePc@NC-1000** exhibited a higher current retention rate of 98.40% after 10 h. Furthermore, the addition of methanol resulted in a significantly larger current retention rate of 94.56% compared to Pt/C (32.40%), demonstrating its excellent methanol tolerance (Fig. 5g).

Based on these results, we present a possible ORR pathway at the Fe-$N_4$ active site in an alkaline solution, as depicted in Fig. 6a, b, and S17 [34]. The process involves a concerted electron transfer (CET) step that leads to the formation of *OOH following the chemical adsorption of $*O_2$. This intermediate subsequently decomposes into *O and $H_2O$. Two additional CET processes generate *O and *OH, enabling the $4e^-$ reduction process and yielding the final product $H_2O$. To further understand the ORR mechanism and facilitate comparative interpretation, a free-energy diagram of the FePc-based electrocatalysts was utilized. As shown in Fig. 6c, at an ORR potential of 1.23 V, pure FePc demonstrates inferior catalytic activity due to the high adsorption energy of each intermediate [35,36]. However, combining FePc with reduced graphene oxide (FePc/RGO) significantly reduces the adsorption energy of the intermediates at nearly every step [37]. It is worth mentioning that in **FePc@NC-1000**, FePc is securely enclosed within *N*-doped carbon, preventing direct exposure of FePc to the solution and enhancing the stability of the Fe-$N_4$ active sites. Furthermore, the electron transfer between FePc and the porous *N*-doped graphitic carbon layers facilitates the adsorption of oxygen and its intermediates, thereby improving ORR activity and durability.

Owing to its high ORR activity and excellent stability, **FePc@NC-1000** is expected to find applications in ZABs (Fig. 7a). Two ZABs connected in series successfully illuminated the LED screen, demonstrating excellent practical performance (Fig. S18). Fig. 7b showed that the **FePc@NC-1000**-based ZAB had an open circuit potential (OCP) of 1.49 V, similar to that of Pt/C (1.51 V). Moreover, it delivered a higher battery power density of 120.37 mW $cm^{-2}$ compared to Pt/C (115.72 mW $cm^{-2}$), indicating good mass transfer kinetics (Fig. 7c). Additionally, a constant-current test was conducted to assess the discharge performance. As depicted in Fig. 7d, the ZABs maintained a relatively stable output voltage from 5 to 100 mA $cm^{-2}$. Furthermore, upon returning the

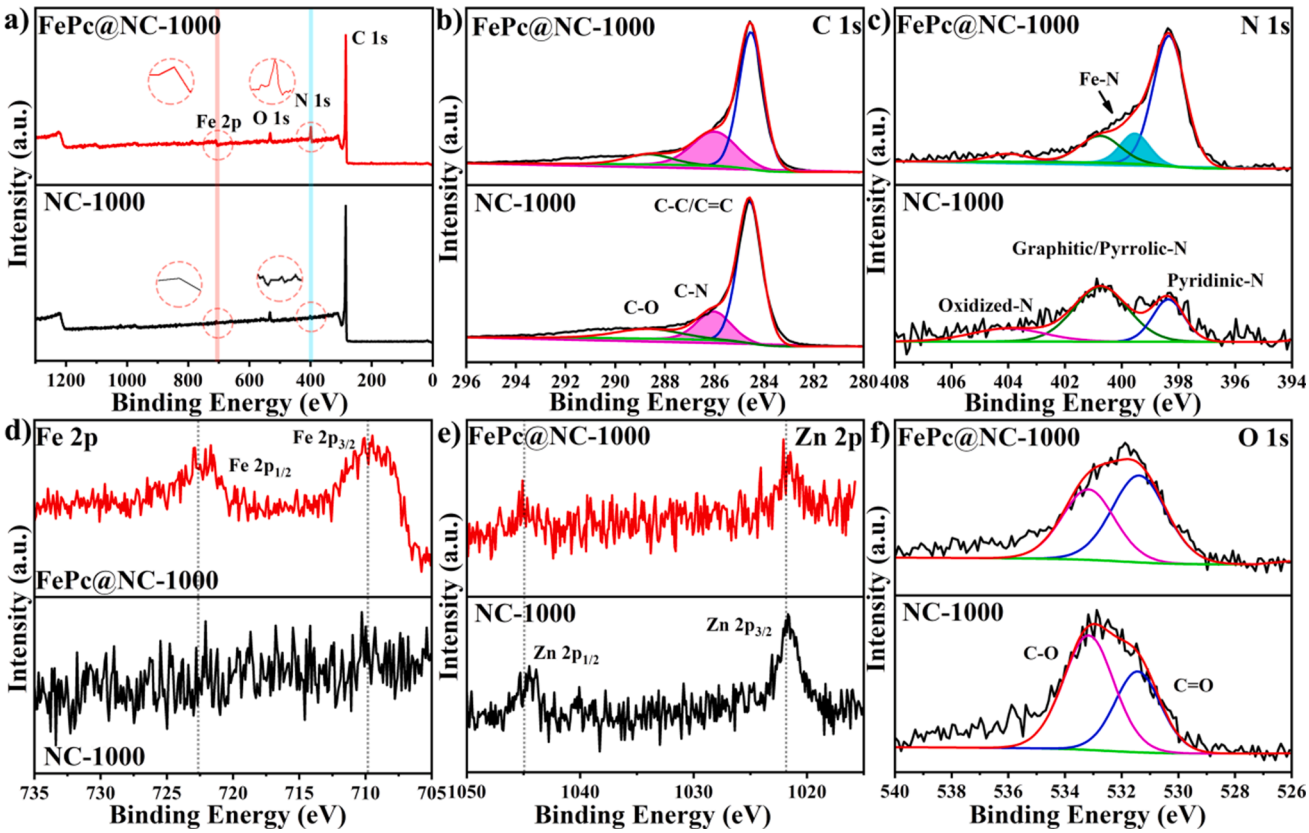


**Fig. 4.** (a) XPS survey spectra. Deconvoluted spectra of (b) C 1s, (c) N 1s, (d) Fe 2p, (e) Zn 2p, and (f) O 1s for **NC-1000** and **FePc@NC-1000**.

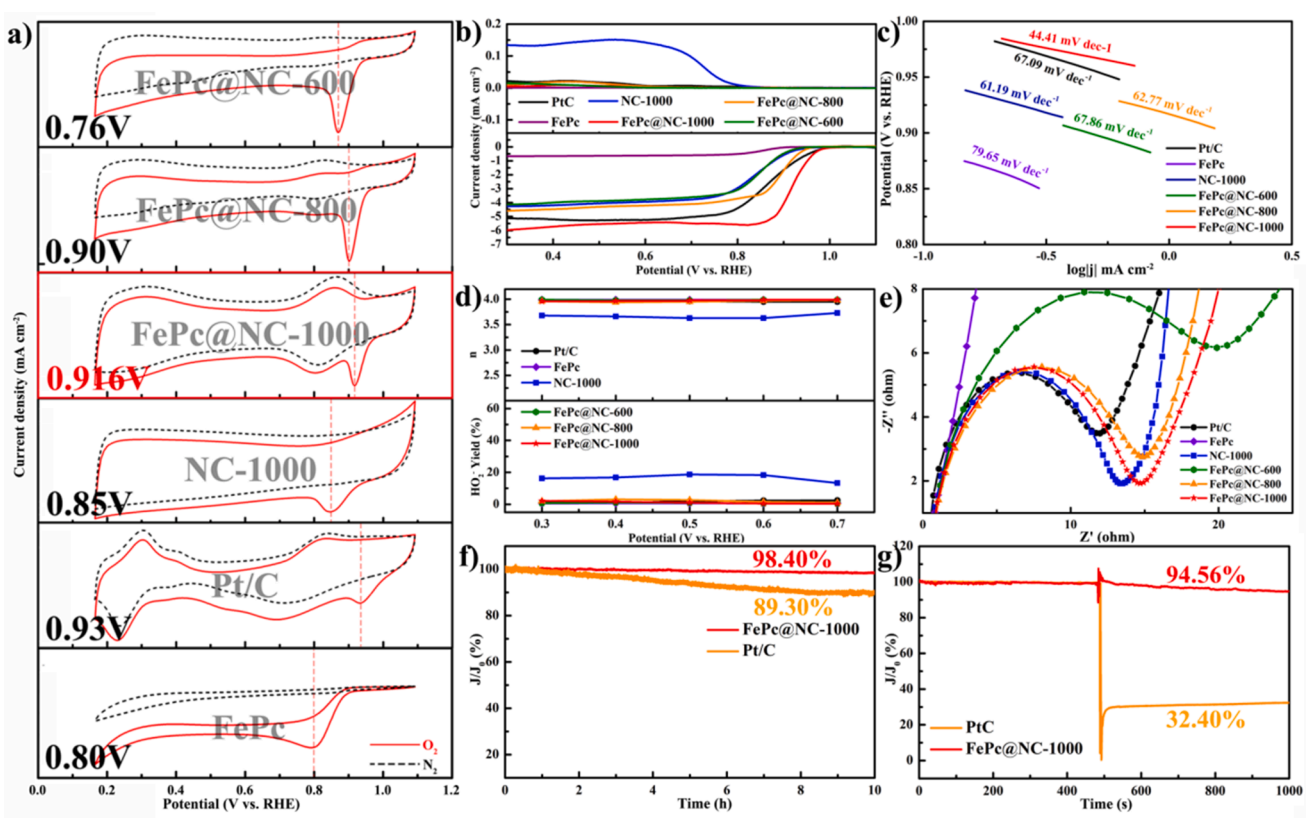


**Fig. 5.** (a) CV profiles, (b) LSV curves, (c) Tafel slopes, (d) *n* and $HO_2^-$ yields, (e) EIS plots for **FePc@NC-600/800/1000**, **NC-1000**, FePc, and Pt/C. (f) stability evaluation, (g) methanol tolerance test for **FePc@NC-1000** and Pt/C.

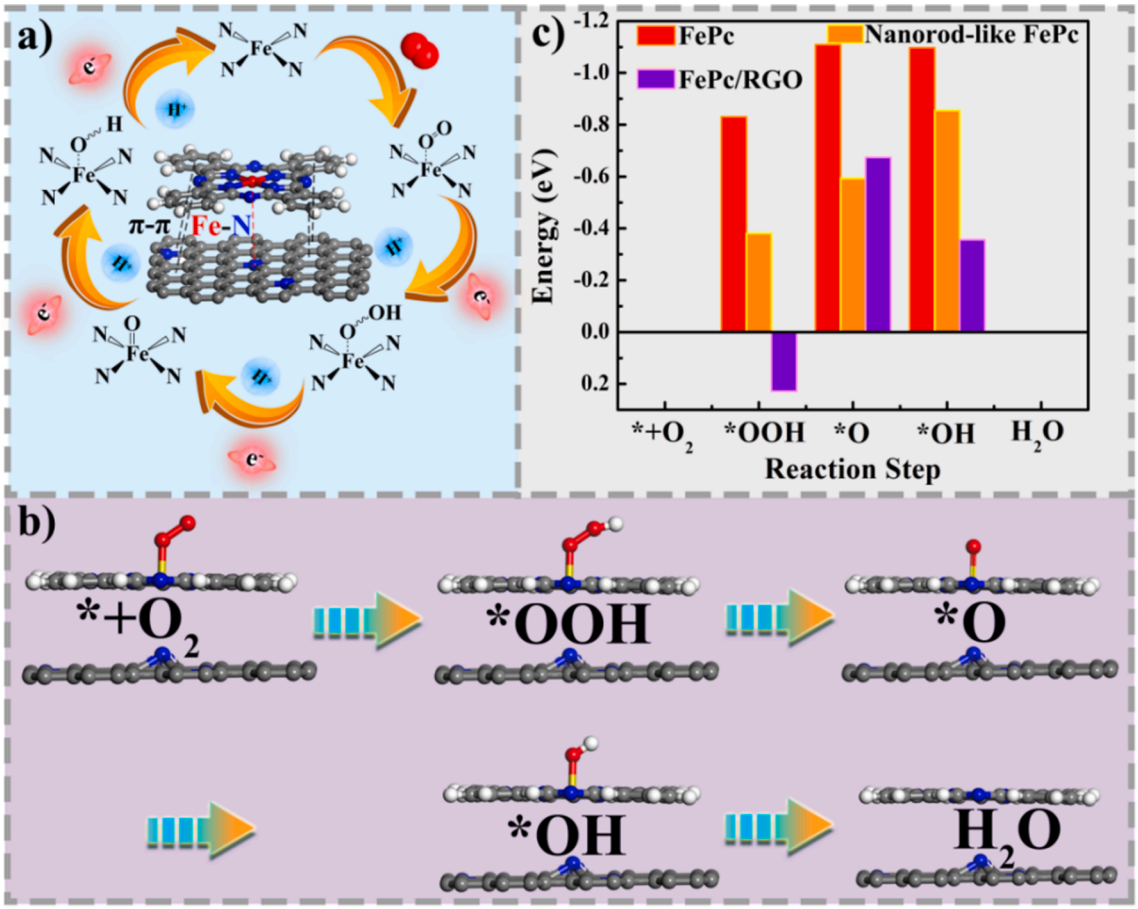


**Fig. 6.** (a) Coordination structures of the Fe-$N_4$ active sites in **FePc@NC.** (b) proposed oxygen reaction path on **FePc@NC.** (c) free energy diagram of 4e$^-$ ORR pathways at FePc-containing catalysts in other work.

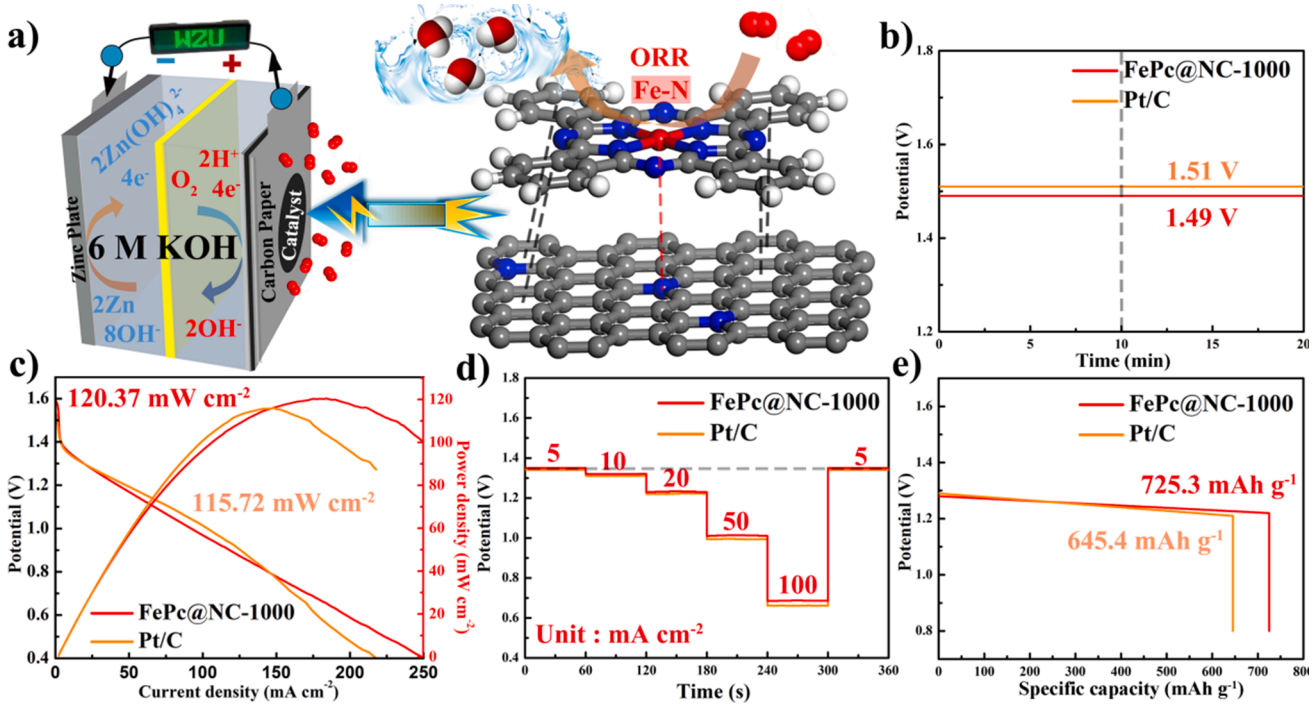


**Fig. 7.** (a) Schematic assembly of a ZAB. (b) OCP curves, (c) polarisation and power density profiles, (d) rate capacity, (e) mass-specific capacity of **FePc@NC-1000** and Pt/C.

current density to 5 mA $cm^{-2}$, the discharge voltage of the ZABs returned to its initial value, indicating high rate capability and durability. Furthermore, the specific capacity of the ZAB based on **FePc@NC-1000** (725.3 mAh $g^{-1}$) is significantly higher than that of Pt/C (645.4 mAh $g^{-1}$) discharged at 10 mA $cm^{-2}$ (Fig. 7e). Overall, the **FePc@NC-1000** proves to be a suitable Pt-free cathode catalyst with considerable application prospects. The exceptional catalytic performance of **FePc@NC-1000** in ZABs can be attributed to the following observations during pyrolysis, effective evaporation of the molten Zn species leads to the formation of numerous pores and N sites. These abundant pores facilitate the adsorption of FePc molecules, while the plentiful N sites effectively anchor FePc molecules through Fe-N interactions. Additionally, the incorporation of N alters the symmetrical Fe-$N_4$ structure of the FePc molecule, thereby enhancing the stability and activity of the Fe active sites. The *N*-doped graphitic carbon exhibits appropriate defect levels and graphitization ratios. The presence of defect sites enables the adsorption of reactants and accelerates the reaction kinetics. Meanwhile, a high degree of graphitization enhances the electron transport capacity, facilitating electron transfer from the carbon substrate to the central active site.

## 4. Conclusion

In this study, a sheet-like Zn-based MOF, **$Zn_2(BDC)_2DABCO$**, has been successfully synthesized and served as a desired precursor for *N*-doped carbon nanosheets. FePc molecules are firmly immobilized onto the MOF-derived porous **NC-1000** through the interaction of Fe-N and π-π stacking, resulting in the preparation of a cost-effective carbon-based catalyst, **FePc@NC-1000**. The N sites within **NC-1000** facilitate the adsorption of FePc and optimize the electron distribution on the Fe-N site by forming electron-deficient Fe. Due to the presence of abundant structural defects and an appropriate degree of graphitization, **FePc@NC-1000** exhibits an increased number of available active centers and promotes the rapid transport of electrons and reaction intermediates. As anticipated, it also demonstrates satisfactory activity for oxygen reduction, with $E_{onset}/E_{1/2}$ values of 0.99/0.86 V and a $J_L$ value of 5.96 mA $cm^{-2}$. Furthermore, the assembled ZAB based on FePc@NC-1000 presents excellent performance and robust stability, comparable to that of state-of-the-art Pt/C catalysts. These results provide a new approach for the development and design of superior electrocatalysts with high ORR catalytic activity and stability, thus contributing to the advancement of green energy technologies.

## CRediT authorship contribution statement

**Anrui Dong:** Methodology, Data curation, Formal analysis, Investigation, Validation, Writing – original draft. **Yu Lin:** Methodology, Data curation, Formal analysis. **Yuanyuan Guo:** Data curation, Formal analysis, Writing – original draft. **Dandan Chen:** Data curation, Formal analysis. **Xian Wang:** Data curation, Formal analysis. **Yongjie Ge:** Investigation, Formal analysis. **Qipeng Li:** Formal analysis, Funding acquisition, Project administration, Writing – review & editing. **Jinjie Qian:** Conceptualization, Formal analysis, Funding acquisition, Investigation, Project administration, Supervision.

## Declaration of Competing Interest

The authors declare that they have no known competing financial interests or personal relationships that could have appeared to influence the work reported in this paper.

## Data availability

Data will be made available on request.

## Acknowledgements

This work was financially supported by National Natural Science Foundation of China (22105147, 21601137), Natural Science Foundation of Zhejiang Province (LQ16B010003), Basic Science and Technology Research Project of Wenzhou, Zhejiang Province (H20220001, G20190007), and the Special Basic Cooperative Research Programs of Yunnan Provincial Undergraduate Universities Association (202101BA070001-042).

## Appendix A. Supplementary material

Supplementary data to this article can be found online at https://doi.org/10.1016/j.jcis.2023.06.043.

## References

[1] F. Chang, W. Gao, J. Guo, P. Chen, Emerging materials and methods toward ammonia-based energy storage and conversion, Adv. Mater. 33 (50) (2021) 2005721.
[2] B. Yang, C. Li, Z. Wang, Q. Dai, Thermoplasmonics in solar energy conversion materials, nanostructured designs, and applications, Adv. Mater. 34 (26) (2022) 2107351.
[3] P. Brockway, A. Owen, L. Brand-Correa, L. Hardt, Estimation of global final-stage energy-return-on-investment for fossil fuels with comparison to renewable energy sources, Nat. Energy 4 (2019) 612–621.
[4] Y. Liu, T. Feng, S. Lu, H. Wang, Y. Xiang, A direct liquid fuel cell with high power density using reduced phosphotungstic acid as redox fuel, Energy Environ. Sci. 5 (1) (2022) 278–284.
[5] K. Meng, B. Chen, H. Zhou, J. Shen, Z. Tu, Experimental investigation on voltage response characteristics of hydrogen-oxygen proton exchange membrane fuel cells under gas starvation, Energy Convers. Manag. 268 (2022) 115973.
[6] Q. Huang, Y. Guo, D. Chen, L. Zhang, T.-T. Li, Y. Hu, J. Qian, S. Huang, Rational construction of ultrafine noble metals onto carbon nanoribbons with efficient oxygen reduction in practical alkaline fuel cell, Chem. Eng. J. 424 (2021) 130336.
[7] X. Wang, J. Li, X. Yang, F. Zhao, Y. Li, D. Zhang, L.-Y. Gan, K.X. Yao, Q. Yuan, Low-coordinated surface sites make truncated Pd tetrahedrons as robust ORR electrocatalysts outperforming Pt for DMFC devices, Nano Res. 15 (9) (2022) 7951–7958.
[8] H. Liu, M. Chen, F. Sun, S. Zaman, M. Wang, H. Wang, Elucidating the correlation between ORR polarization curves and kinetics at metal-electrolyte interfaces, ACS Appl. Mater. Interfaces 14 (11) (2022) 13891–13903.
[9] J. Fonseca, T. Gong, L. Jiao, H.-L. Jiang, Metal-organic frameworks (MOFs) beyond crystallinity amorphous MOFs, MOF liquids and MOF glasses, J. Mater. Chem. A 9 (17) (2021) 10562–10611.
[10] K. Ikigaki, K. Okada, Y. Tokudome, T. Toyao, P. Falcaro, C.J. Doonan, M. Takahashi, MOF-on-MOF oriented growth of multiple layered thin films of metal-organic frameworks, Angew. Chem. Int. Ed. 58 (21) (2019) 6886–6890.
[11] C. Pettinari, R. Pettinari, C. Di Nicola, A. Tombesi, S. Scuri, F. Marchetti, Antimicrobial MOFs, Coord. Chem. Rev. 446 (2021) 214121.
[12] Q. Li, Z. Dai, J. Wu, W. Liu, T. Di, R. Jiang, X. Zheng, W. Wang, X. Ji, P. Li, Z. Xu, X. Qu, Z. Xu, J. Zhou, Fabrication of ordered macro-microporous single-crystalline MOF and its derivative carbon material for supercapacitor, Adv. Energy Mater. 10 (33) (2020) 1903750.
[13] J. Ding, Y. Tang, S. Zheng, S. Zhang, H. Xue, Q. Kong, H. Pang, The synthesis of MOF derived carbon and its application in water treatment, Nano Res. 15 (8) (2022) 6793–6818.
[14] S. Payra, K. Likhitha Reddy, R.S. Sharma, S. Singh, S. Roy, A trade-off between adsorption and photocatalysis over ZIF-derived composite, J. Hazard. Mater. 393 (2020) 122491.
[15] C. Ouyang, L. Zheng, Q. Zhang, X. Wang, A simple preheating-pyrolysis strategy leading to superior oxygen reduction reaction activity in Fe-N/carbon black, Adv. Mater. 34 (40) (2022) 2205372.
[16] W.Y. Noh, J. Mun, Y. Lee, E.M. Kim, Y.K. Kim, K.Y. Kim, H.Y. Jeong, J.H. Lee, H.-K. Song, G. Lee, J.S. Lee, Molecularly engineered carbon platform to anchor edge-hosted single-atomic M-N/C (M = Fe Co, Ni, Cu) electrocatalysts of outstanding durability, ACS Catal. 12 (13) (2022) 7994–8006.
[17] Z.-Y. Mei, S. Cai, G. Zhao, X. Zou, Y. Fu, J. Jiang, Q.i. An, M. Li, T. Liu, H. Guo, Boosting the ORR active and Zn-air battery performance through ameliorating the coordination environment of iron phthalocyanine, Chem. Eng. J. 430 (2022) 132691.
[18] A. Kumar, Y. Zhang, Y. Jia, W. Liu, X. Sun, Redox chemistry of $N_4$-$Fe^{2+}$ in iron phthalocyanines for oxygen reduction reaction, Chin. J. Catal. 42 (8) (2021) 1404–1412.
[19] W. Xia, Z. Hou, J. Tang, J. Li, W. Chaikittisilp, Y. Kim, K. Muraoka, H. Zhang, J. He, B. Han, Y. Yamauchi, Materials informatics-guided superior electrocatalyst A case of pyrolysis-free single-atom coordinated with N-graphene nanomesh, Nano Energy 94 (2022) 106868.
[20] X. Yu, S. Lai, S. Xin, S. Chen, X. Zhang, X. She, T. Zhan, X. Zhao, D. Yang, Coupling of iron phthalocyanine at carbon defect site via π-π stacking for enhanced oxygen reduction reaction, Appl. Catal. B. 280 (2021) 119437.

[21] X. Wang, A. Dong, Y. Hu, J. Qian, S. Huang, A review of recent work on using metal-organic frameworks to grow carbon nanotubes, Chem. Commun. 56 (74) (2020) 10809–10823.
[22] D. Dybtsev, H. Chun, K. Kim, Host-GuestSystemsRigid and flexible A highly porous metal-organic framework with unusual guest-dependent dynamic behavior, Angew. Chem. Int. Ed. 43 (2004) 5033–5036.
[23] O. Farha, J. Hupp, Rational design, synthesis, purification, and activation of metal-organic framework materials, Acc. Chem. Res. 43 (8) (2010) 1166–1175.
[24] T. Xiao, D. Liu, The most advanced synthesis and a wide range of applications of MOF-74 and its derivatives, Micropor. Mesopor. Mat. 283 (2019) 88–103.
[25] T. Chang, Z. Li, G. Yun, Y. Jia, H. Yang, Enhanced photocatalytic activity of ZnO/CuO nanocomposites synthesized by hydrothermal method, Nano-Micro Lett. 5 (3) (2013) 163–168.
[26] Y. Guo, Q.i. Huang, J. Ding, L.i. Zhong, T.-T. Li, J. Pan, Y. Hu, J. Qian, S. Huang, CoMo carbide/nitride from bimetallic MOF precursors for enhanced OER performance, Int. J. Hydrog. Energy 46 (43) (2021) 22268–22276.
[27] C. Han, X. Zhang, T. Li, Y. Hu, J. Qian, Carbon nanotubes grown on CuO nanoparticle-decorated porous carbon microparticles for water oxidation, ACS Appl. Nano Mater. 4 (2021) 12119–12126.
[28] D. Chen, Q. Huang, J. Ding, T. Li, D. Yu, H. Nie, J. Qian, Z. Yang, Heteroepitaxial metal-organic frameworks derived cobalt and nitrogen codoped carbon nanosheets to boost oxygen reduction, J. Colloid Interface Sci. 623 (2022) 1210–1219.
[29] F. Tan, W. Li, J. Wang, C. Min, Z. Li, B. Zhang, X. Zheng, L. Li, L. Zhang, L. Zhou, Q. Shi, X. Yang, Clarifying the critical roles of iron in boosting oxygen reduction Single Fe atoms anchored on carbon vacancies as efficient active sites, Appl. Catal. B. 305 (2022) 121035.
[30] Q. Wang, R. Lu, Y. Yang, X. Li, G. Chen, L.u. Shang, L. Peng, D. Sun-Waterhouse, B. C.C. Cowie, X. Meng, Y. Zhao, T. Zhang, G.I.N. Waterhouse, Tailoring the microenvironment in Fe-N-C electrocatalysts for optimal oxygen reduction reaction performance, Sci. Bull. 67 (12) (2022) 1264–1273.
[31] T. Marshall-Roth, N. Libretto, A. Wrobel, K. Anderton, M. Pegis, N. Ricke, T. Voorhis, J. Miller, Y. Surendranath, A pyridinic Fe-$N_4$ macrocycle models the active sites in Fe/N-doped carbon electrocatalysts, Nat. Commun. 11 (2020) 5283.
[32] J. Kim, Y. Sa, H. Jeong, S. Joo, Roles of Fe-$N_x$ and Fe-$Fe_3$[email protected] species in Fe-N/C electrocatalysts for oxygen reduction reaction, ACS Appl. Mater. Interfaces 9 (2017) 9567–9575.
[33] L. Lan, J. Li, Y. Yang, L. Zhang, L. Zhang, Q. Fu, X. Zhu, Q. Liao, Enhanced Fe-N active site formation through interfacial energy control of precursor impregnation solution for the air cathode of membraneless direct formate fuel cells, Carbon 189 (2022) 240–250.
[34] W. Wang, Q. Jia, S. Mukerjee, S. Chen, Recent Insights into the oxygen-reduction electrocatalysis of Fe/N/C materials, ACS Catal. 9 (11) (2019) 10126–10141.
[35] H. Abe, Y. Hirai, S. Ikeda, Y. Matsuo, H. Matsuyama, J. Nakamura, T. Matsue, H. Yabu, Fe azaphthalocyanine unimolecular layers (Fe AzULs) on carbon nanotubes for realizing highly active oxygen reduction reaction (ORR) catalytic electrodes, NPG Asia Mater. 11 (2019) 57.
[36] A. Kumar, K. Sun, X. Duan, S. Tian, X. Sun, Construction of dual-atom Fe via face-to-face assembly of molecular phthalocyanine for superior oxygen reduction reaction, Chem. Mater. 34 (12) (2022) 5598–5606.
[37] J. Guo, X. Yan, Q. Liu, Q. Li, X. Xu, L. Kang, Z. Cao, G. Chai, J. Chen, Y. Wang, J. Yao, The synthesis and synergistic catalysis of iron phthalocyanine and its graphene-based axial complex for enhanced oxygen reduction, Nano Energy 46 (2018) 347–355.